

Image-Based Cardiac Phase Retrieval in Intravascular Ultrasound Sequences

Aura Hernández-Sabaté, Debora Gil, Jaume Garcia-Barnés, and Enric Martí

Abstract—Longitudinal motion during *in vivo* pullbacks acquisition of intravascular ultrasound (IVUS) sequences is a major artifact for 3-D exploring of coronary arteries. Most current techniques are based on the electrocardiogram (ECG) signal to obtain a gated pullback without longitudinal motion by using specific hardware or the ECG signal itself. We present an image-based approach for cardiac phase retrieval from coronary IVUS sequences without an ECG signal. A signal reflecting cardiac motion is computed by exploring the image intensity local mean evolution. The signal is filtered by a band-pass filter centered at the main cardiac frequency. Phase is retrieved by computing signal extrema. The average frame processing time using our setup is 36 ms. Comparison to manually sampled sequences encourages a deeper study comparing them to ECG signals.

I. INTRODUCTION

A major concern during *in vivo* coronary intravascular ultrasound (IVUS) pullbacks is that forward and backward longitudinal translation along the catheter axis [1] results in a swinging effect on the reconstructed images. Such motion produces a sequence block with spatially shuffled frames. The shuffled sequence does not provide a faithful 3-D reconstruction, hinders volumetric measurements, and affects the appearance of longitudinal views.

Fig. 1 illustrates the swinging effect caused by off-plane dynamics at a side branch. At the top of the figure, there are three IVUS images at different parts of the same cardiac cycle. The side-branch (in the second quadrant of images) is marked with a circle. Because of in- and out-of-plane cardiac motion, the side branch is located at different distances from the main artery along a given cardiac cycle: proximal to the main branch at frame A, distal to it at frame B (where it is hardly visible), and joining it at frame C. The longitudinal cut shown in the bottom image of Fig. 1 corresponds to the angle indicated with white solid lines in the top IVUS images. Their positions in the sequence are given by dashed lines (also labeled A, B, C) in the longitudinal cut. The swinging motion of the side-branch is reflected in the longitudinal cut upper profile, which shows the characteristic saw-tooth shape.

Longitudinal motion artifacts might be overcome by electrocardiogram (ECG)-gating approaches, which pro-

duce a static sequence synchronized with a given part of the cardiac cycle. Synchronization can be performed either on-line (prospective triggering) during acquisitions [2] or off-line (retrospective samplings) by processing a standard non-gated sequence [3].

An ECG-gated system for prospective acquisition of images acquires only one frame per cycle, which might increase acquisition time up to 3 times [4]. Furthermore, on-line ECG-gating provides only one single sequence at a given cardiac phase. This reduces the potential of IVUS for studying bio-mechanical vessel properties (such as elastography), because they require analysis of vessel deformation at different times of the cardiac cycle [5]–[8].

These issues have motivated development of retrospective sampling of sequences. Sequence stabilization is achieved by sampling sequences always at the same part of the cardiac phase. Cardiac phase is usually defined by means of the interval between two consecutive R-waves in ECG signals [9]. However, ECG-signals are usually registered externally, by placing electrodes on the patient's chest. A single catheter for registering ultrasound and ECG-signal cannot be introduced because there is a potential differential and a reference signal on another point is needed. It follows that synchronized acquisition of IVUS frames and ECG-signal is not feasible in clinical practice [9]. Also, to our knowledge, there is not a clear criterion for determining the optimal part of the cardiac cycle for getting maximal inter-frame stability in IVUS [9], [10]. Although most approaches use the 0% point, which corresponds to end-diastole, it is still controversial whether this fraction provides the most stable sequences [9], [11]. This has recently motivated exploration of the potential of image processing techniques for retrieving cardiac phase [12]–[15] from non-gated sequences without ECG-signal.

Existing strategies for image-based gating follow the scheme outlined in Fig. 2. First, a signal reflecting cardiac motion is extracted from IVUS sequences. Second, the signal is filtered (in the Fourier domain) to remove non-cardiac phenomena and artifacts. Finally, a suitable sampling of the filtered signal is used to retrieve cardiac phase. All authors agree on using the extrema of a signal reflecting cardiac motion for sampling it at the same part of the cardiac phase. The main differences among existing algorithms and, thus, the clue for an accurate cardiac phase retrieval, are on the computation of the cardiac signal and its further filtering.

Cardiac phase is obtained by exploring temporal changes of either vessel structures (lumen size) [12], [13] or image gray-level [14], [16], [17]. Given that segmentation of IVUS images is not straightforward, exploring

Manuscript received July 24, 2009; accepted October 4, 2010. This work was supported by the Spanish projects PI071188, TIN2009-13618 and CONSOLIDER-INGENIO 2010 (CSD2007-00018). D. Gil has been supported by The Ramon y Cajal Program.

The authors are with the Computer Vision Center and Department of Computer Science, Universitat Autònoma de Barcelona, Bellaterra, Spain (e-mail: aura,debora@cvc.uab.cat).

Digital Object Identifier 10.1109/TUFFC.2011.1774

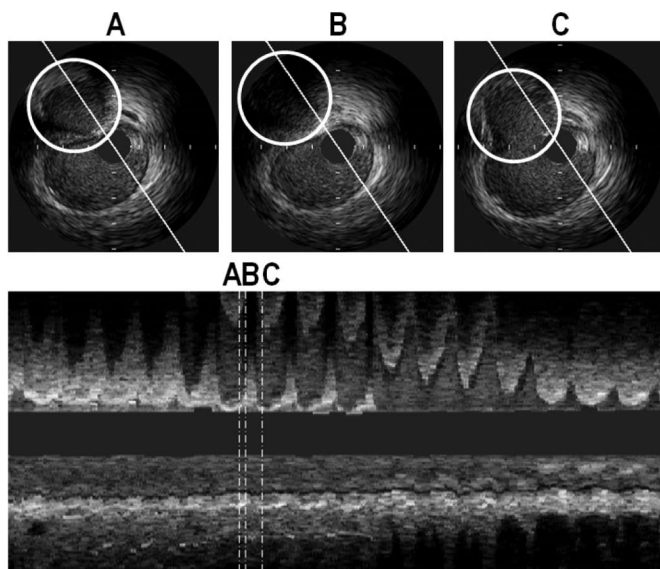


Fig. 1. Swinging effect in longitudinal cuts. White lines at the same angle in frames A, B, C (top images) correspond to the vertical white lines in the longitudinal cut (bottom image). The swinging bifurcation can be clearly noticed in both cross-sections and longitudinal cut.

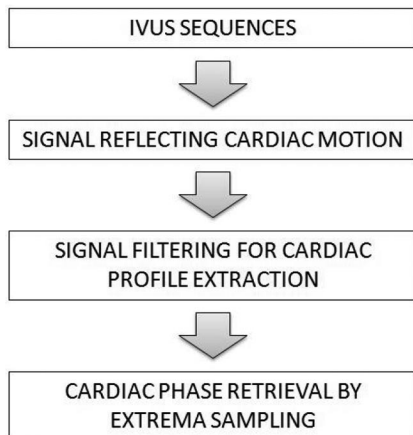


Fig. 2. Pipeline for image-based cardiac phase retrieval.

vessel structures requires manual intervention. Nadkarni *et al.* [12] compute the changes of lumen size by means of the area enclosed by a manual segmentation of vessel lumen. Zhu *et al.* [13] explore lumen size evolution by computing gray-level statistics inside a manually defined ROI. Image intensity methods do not require user intervention, because they do not need identification of vessel structures. However, the choice of the similarity measure detecting changes between consecutive frames is a delicate step. Current approaches use (global) similarity measures taking into account all image pixels. We remit the reader to [14] for a report exploring the performance of different similarity measures. Such study points that measures based on information theory are better suited to the problem. The methods presented in [16] and [17] use cross-correlation to compute dissimilarity matrices, which are used to find corresponding frames. A main limitation is

the complexity in algorithms caused by the construction of dissimilarity matrices or measures coming from information theory. Furthermore, although the first quantitative results reported in [14] and [16] are very promising, we consider that global similarity measures are sensitive to texture changes and motionless regions [18].

Regarding the filter used, all approaches agree on using a band-pass filter for discarding frequencies not contributing to cardiac motion. Current approaches use wavelet filters such as Butterworth [13] and Daubechies [14]. Heart rate variability spreads (cardiac) frequencies around the main cardiac frequency in the Fourier domain. The more irregularities in periodicity we have, the more spread around the theoretic harmonic the Fourier development is. It follows that decay and support of the filter is crucial for a proper image-based ECG sampling in pathological cases and large segments. An analysis of the best filter and band-width is the first step for a robust cardiac phase retrieval in pathological cases and segments of different lengths, but has not been addressed so far.

In this paper, we contribute to image-based cardiac phase retrieval in two aspects: computation of the signal reflecting cardiac motion and exploring, for the first time, the impact of the band-pass filter shape on the sampling accuracy. The proposed signal reflecting cardiac motion is based on the changes that the gray-level local mean undergoes along the sequence. Such local approach minimizes the impact of texture and motionless regions and provides a fully automated method close to real time. Regarding the band-pass filter, two families (with different decays and support) are proposed: Gaussian and Butterworth. We present a statistical methodology for determining which band-pass filter profile is better suited for cardiac phase retrieval.

The remainder of the paper is structured as follows. In Section II, we describe our process for extracting the cardiac signal. In Section III, we describe the validation protocol and the test to determine which of the proposed filters is the best for cardiac phase retrieval in terms of a significant statistical difference. Experiments on *in vivo* sequences are described in Section IV. Finally, discussions and conclusions are explained in Sections V and VI.

II. CARDIAC PHASE RETRIEVAL

According to clinical reports [19], maximum and minimum lumen areas correspond to end-systole and end-diastole. Following the general scheme of Fig. 2, we split our method into three steps:

- 1) Extraction of a signal reflecting cardiac motion. By the physical coupling [20], luminal area evolution is synchronized to other vessel cardiac phenomena, such as tissue motion. We propose using the latter to retrieve a signal reflecting motion. By the properties of ultrasonic images, pixel intensity is related to the density of mass which we approximate by the image

local mean (LM). The evolution of the LM along the sequence provides, for each pixel, a 1-dimensional signal. Vessel motion is not reflected in the whole vessel section, but only at regions presenting (abrupt) changes in image intensity. In the context of IVUS images, such points correspond to transition areas across tissue and structures of different nature (e.g., lumen-vessel wall interface or calcium plaque borders). However, arterial morphologic and geometric changes and breathing might corrupt the LM periodic profile induced by heart beats. It follows that the signal reflecting cardiac motion should only combine LM signals extracted at pixels properly reflecting cardiac dynamics. Such signals are selected by optical filtering [21] of the LM Fourier transform, \widehat{LM} .

- 2) Signal filtering for cardiac profile extraction. Cardiac phase is not constant along the pullback. As well, the cardiac profile contains cardiac information, but also contains other non-cardiac phenomena. This suggests that the profile reflecting cardiac motion should be filtered. Following the literature, we use a band-pass filter to control the regularity of the signal. Because of heart rate variability, the decay and support of the filter is crucial for a proper image-based ECG sampling. We consider several filters covering different supports and decays to explore which one is better suited for cardiac phase retrieval.
- 3) Cardiac phase retrieval. Minimums and maximums of the filtered signals retrieve cardiac phase at the same fraction (not necessarily end-diastole) of the cardiac cycle [9], [14]. We would like to note that sampling synchronized to a cardiac phase different from end-diastole might be beneficial for producing stable sequences in two aspects [9], [11]. First, given that sequences include frames covering all cardiac phases, we can retrieve segments at any cardiac phase (in particular end-diastole) by means of a shift representing the same fraction of the cycle. Second, a sampling corresponding to extreme phenomena in images might yield better inter-frame stabilization of the static model of the vessel.

The extraction of the cardiac frequency is necessary for the first two steps. In the case of a constant heart rate, the LM would be a pure periodic signal. Pure periodic signals have a discrete Fourier series given by multiples (called harmonics) of a principal frequency. It follows that, in such case, the cardiac frequency is uniquely defined by the principal frequency. Any variation in heart rate spreads frequencies of the Fourier series around the theoretic harmonic. This produces a harmonic peak including all frequencies that contribute to the principal periodic motion along its sequence. For each Fourier series, \widehat{LM} , we define its cardiac frequency as the maximum of the first harmonic peak in the interval (45, 200) rpm [22]. For the sake of an efficient algorithm, the local maximum is approximated by the global maximum in such interval [23]. For

each pixel, the LM profile is a combination of several contributions [18]. Heart beat and breathing induce a periodic variation of different principal harmonics. Additionally, morphologic and geometric arterial changes have a broad and wide spectrum with principal amplitudes at low-band frequencies. It follows that for those LM signals presenting predominantly breath and morphologic components, our estimation of the cardiac frequency is biased. Because they constitute a small set of all image pixels, the average of LM cardiac frequencies for a uniform sampling of pixels constitutes a reliable approximation to cardiac frequency, which we denote ω_c .

A. Step 1—Extraction of a Signal Reflecting Cardiac Motion

Following [24], we compute LM images by 2-D convolution of the original sequence frames with an $n_P \times n_P$ averaging kernel, κ :

$$LM(x, y, t) := \kappa(x, y) * I(x, y, t),$$

where $I(x, y, t)$ denotes the original sequence and the kernel κ is an $n_P \times n_P$ matrix with entries $(\kappa_{ij})_{ij} = 1/(n_P^2)$. In our case, we used an (empirically set) 9×9 kernel. The local average LM is a sequence reflecting the density of mass of the underlying tissue. Because of cardiac motion (both longitudinal and in-plane) and other dynamics (such as breathing), an image pixel does not necessarily correspond to the same material point on the artery. It follows that the time-dependant 1-D signal, defined by fixing the position of a pixel, reflects the changes in the material point's mass density.

Fig. 3 shows LM evolution for three different pixels: from left to right, a pixel on a calcified plaque (identified in red), a pixel at luminal cavity close to lumen-vessel interface (identified in green), and a motionless pixel (identified in magenta). Images on the left-hand side show the original IVUS sequence (top image) and the one corresponding to LM (bottom image). The positions of the three pixels are marked with asterisks. Points reflecting cardiac motion correspond to the projection of such points onto the image plane (usually the first sequence frame). It follows that they might not be on a transition border on the image chosen, but later on in the sequence. The graphs on the right side of Fig. 3 plot LM profiles along the pullback for (from top to bottom) calcified plaque (longitudinal) transition, lumen-vessel interface, and motionless pixels. The red pixel on the calcified plaque reflects longitudinal motion by the 3-D transition between calcified and non-calcified structures along the pullback (the plaque crosses the position of the red pixel because of cardiac motion). This is reflected in the top plot on the right-hand side. The green pixel is close to the lumen-wall interface, though located inside the luminal cavity. Therefore, in the original IVUS sequence, the lumen-wall interface does not cross its position at any frame. In the LM sequence, the 9×9 window used for its computation

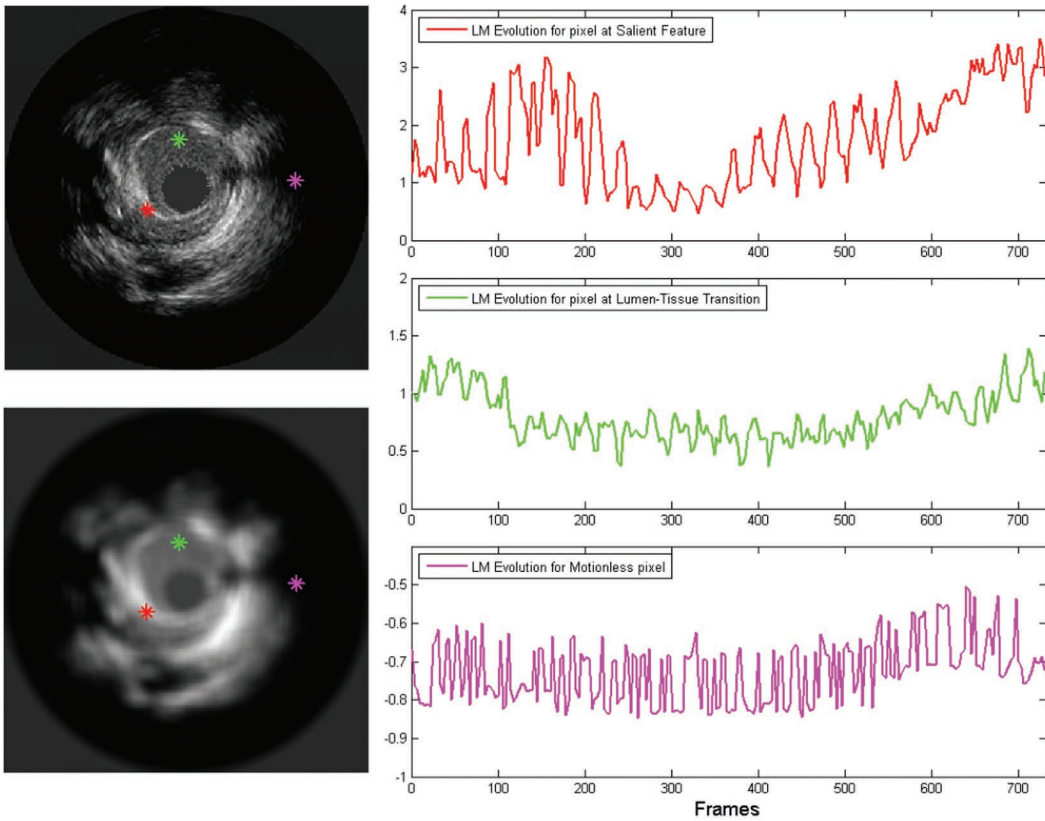


Fig. 3. Local mean evolution of different pixels. On the left, the original intravascular ultrasound sequence (top image) and the one corresponding to local mean (bottom image). On the right, the graphics of the evolution of three pixels, a pixel at a salient feature (top), a pixel at lumen-tissue transition (middle), and a motionless pixel (bottom).

extends the scope of interface regions. This is reflected in a periodic pattern (although weaker than the calcium pixel) in the middle LM plot on the right-hand side. Finally, the motionless pixel located in a background shadow does not reflect any persistent pattern in any of the sequences (original or LM).

The impact of background noise and textured areas, as well as non-cardiac dynamic phenomena (breathing, artery torsion, etc.) is reduced in two stages. First, we discard motionless pixels and, then we select pixels presenting a clear cardiac periodic motion.

Motionless pixels are discarded by considering those points with $\widehat{\text{LM}}$ cardiac amplitude over the 80% percentile of all $\widehat{\text{LM}}$ cardiac amplitudes [24]. The amplitude filter removes those LM signals in which cardiac amplitude was biased from the true one. The remaining LM signals, after motionless pixels removal, should present a periodic profile. Therefore, their Fourier transform $\widehat{\text{LM}}$ should be as close to a discrete series (given by ω_c multiples) as possible. However, other dynamic phenomena, such as breathing, morphological changes along the sequence, as well as irregularities in heart beat are prone to reduce the cardiac amplitude and, thus, might distort the ideal discrete profile. Such signals do not properly reflect cardiac motion and should be excluded. Irregularities in periodic profiles make the theoretic harmonic peaks spread around ω_c harmonics. The more irregular the profile is, the more spread

the frequencies are. We remove such signals by means of an optical filtering [21] centered at the principal harmonic ω_c . Optical filtering is a technique widely used in electron crystallography to discard harmonics corrupted with noise. Optical filtering selects only those harmonics presenting a prominent peak. The degree of peak of the harmonic is given by the normalized difference between the amplitude achieved at the harmonic and an average of amplitudes in a neighborhood I_{ω_c} centered at the principal harmonic:

$$\text{OF}(\omega_c) = \frac{|\widehat{\text{LM}}(\omega_c)|}{S} - \frac{1}{N \times S} \sum_{x \in I_{\omega_c} \setminus \omega_c} |\widehat{\text{LM}}(x)|, \quad (1)$$

where $S = \sum_{x \in I_{\omega_c}} |\widehat{\text{LM}}(x)|$ and N is the number of harmonics in I_{ω_c} . Only LM signals with OF above a given threshold [18] contribute to the average defining the signal reflecting cardiac motion. The length of I_{ω_c} should not be larger than the distance between consecutive harmonics, which is given by $k\omega_c - (k+1)\omega_c = \omega_c$, in our case. To take into account all possible contributions, we consider the full interval $I_{\omega_c} = (\omega_c - \omega_c/2, \omega_c + \omega_c/2)$.

Fig. 4 illustrates the removal of those pixels with a non-cardiac profile. The top graphics show the result of removing pixels with a low LM signal. On the left hand side, we show the uniform sampling of pixels considered to compute LM along the sequence. The Fourier development

$\widehat{\text{LM}}$ for three representative pixels (circled in red on the left image) are shown in the central plots. The top plot corresponds to a background pixel with no motion information. Plots in the black box correspond to pixels reflecting motion; the one in the middle shows a well-defined motion pattern and the one at the bottom shows an erratic motion profile. The selection of pixels over the 80% percentile of all $\widehat{\text{LM}}(\omega_c)$ is given on the right side image. We would like to note that transition pixels form a 3-D surface along the vessel. Points reflecting cardiac motion correspond to the projection of such points onto the image plane shown in the figure. It follows that they might not be on a transition border on the image chosen, but later on in the sequence. Because the Fourier spectrum takes into account all frames, their cardiac peak is well defined as long as they belong to lumen-wall interface in a large enough number of frames. Graphics at the bottom of Fig. 4 show the removal of corrupted motion profiles. On the left-hand side we show the pixels selected after the removal of motionless signals. Central plots show $\widehat{\text{LM}}$ profiles for the two kinds of remaining pixels. The top plot shows a pixel properly reflecting cardiac motion and, thus, it has a regular profile. The bottom plot shows a pixel not reflecting an accurate cardiac motion, and, thus, it has an irregular profile. Its erratic pattern is better appreciated in the close-up. Pixels selected by optical filtering are shown in the right image.

Fig. 5 plots the signal reflecting cardiac motion on a longitudinal cut. Observe that the most prominent extrema (maximums and minimums) of the signal reflecting cardiac motion correspond to maximums and minimums of the longitudinal cut profile. We would like to note that the position of the extreme of the signal reflecting motion is prone to be corrupted (deviated) by noise, texture, and non-cardiac dynamics. It follows that the signal should be filtered before computation of the extrema.

B. Step 2—Signal Filtering for Cardiac Profile Extraction

Even in healthy subjects, cardiac frequency does not remain constant along the sequence, which introduces (among other phenomena) irregularities in the Fourier transform of the cardiac motion profile. Such irregularities distort the cardiac signal and corrupt the location of local extrema in the signal reflecting cardiac motion. It follows that the signal should be filtered. Following the literature, we filter the cardiac profile with a band-pass filter. We consider two families of band-pass filters centered at ω_c : Butterworth (*B*) [13] and Gaussian-based (*G*) [14]. filters are given in Fourier domain by the formulae:

$$B(\omega) = B_{n,\delta}(\omega) = \frac{1}{\sqrt{1 + \left(\frac{|\omega| - \omega_c}{0.6\Delta\omega}\right)^{2n}}}, \quad \text{for } \Delta\omega = h\omega_c,$$

$$G(\omega) = G_\delta(\omega) = \frac{1}{\sigma\sqrt{2\pi}} e^{-(|\omega| - \omega_c)^2 / (2\sigma^2)}, \quad \text{for } \sigma = \delta\omega_c.$$

For Butterworth, n is related to the filter decay and δ is proportional to its support. Meanwhile for Gaussian-based, the decay cannot be handled (it is always exponential) and only its support may be tuned by its deviation, σ .

The real part of the inverse Fourier transform of the filtered cardiac profile is a smooth signal for the cardiac phase retrieval. Regardless of the filter used, we denote it by f .

C. Step 3—Cardiac Phase Retrieval

Maximums and minimums of the filtered signal give a sampling at the same part of the cardiac cycle and, thus, retrieve cardiac phase for each selected pixel. The extrema in the time domain of a signal f are given by the zero crossings of its first derivative, $f' = 0$. Because, in our case, f is a differentiable function of compact support, its derivatives can be analytically computed in Fourier space using the formula [25]

$$\widehat{f^{(k)}}(\omega) = (2\pi i\omega)^k \hat{f}(\omega). \quad (2)$$

The inverse Fourier transform of (2) for $k = 1$ gives the first derivative of f in the time domain. Zero crossings are computed by changes in sign of f' .

III. VALIDATION PROTOCOL

The methodologies have been validated in 22 vessel segments 420 to 690 frames long (approximately 7 to 11.5 mm) from the IVUS database of InCor (Hospital das Clínicas da Faculdade de Medicina, Universidade de São Paulo). Sequences were recorded with a Galaxy digital imaging console (Boston Scientific Corp., Natick, MA) at 40 MHz, with a rotating single transducer and constant pullback speed of 0.5 mm/s. The digitization rate was 30 fps.

Automatic samplings were compared with the frames achieving extreme lumen areas. These extrema were manually detected by exploring longitudinal cuts and selecting minimums and maximums of intima/lumen and media-adventitia transition profiles. We have considered 3 quality scores and 2 different statistics for reporting results.

Accuracy of each ECG-gating method is given the average along the sequence of the absolute difference between the positions of automatically and manually sampled frames. Distances between manually detected frames and automatic ones were computed as the absolute differences between their positions. That is, if s^k and \tilde{s}^k are frame positions in the sequence for a manual and automatic sampling, respectively, we define their distance:

$$E^k = |s^k - \tilde{s}^k|.$$

The distances for all frames provide a distance map for each sequence. We retrieve a single quantity for the

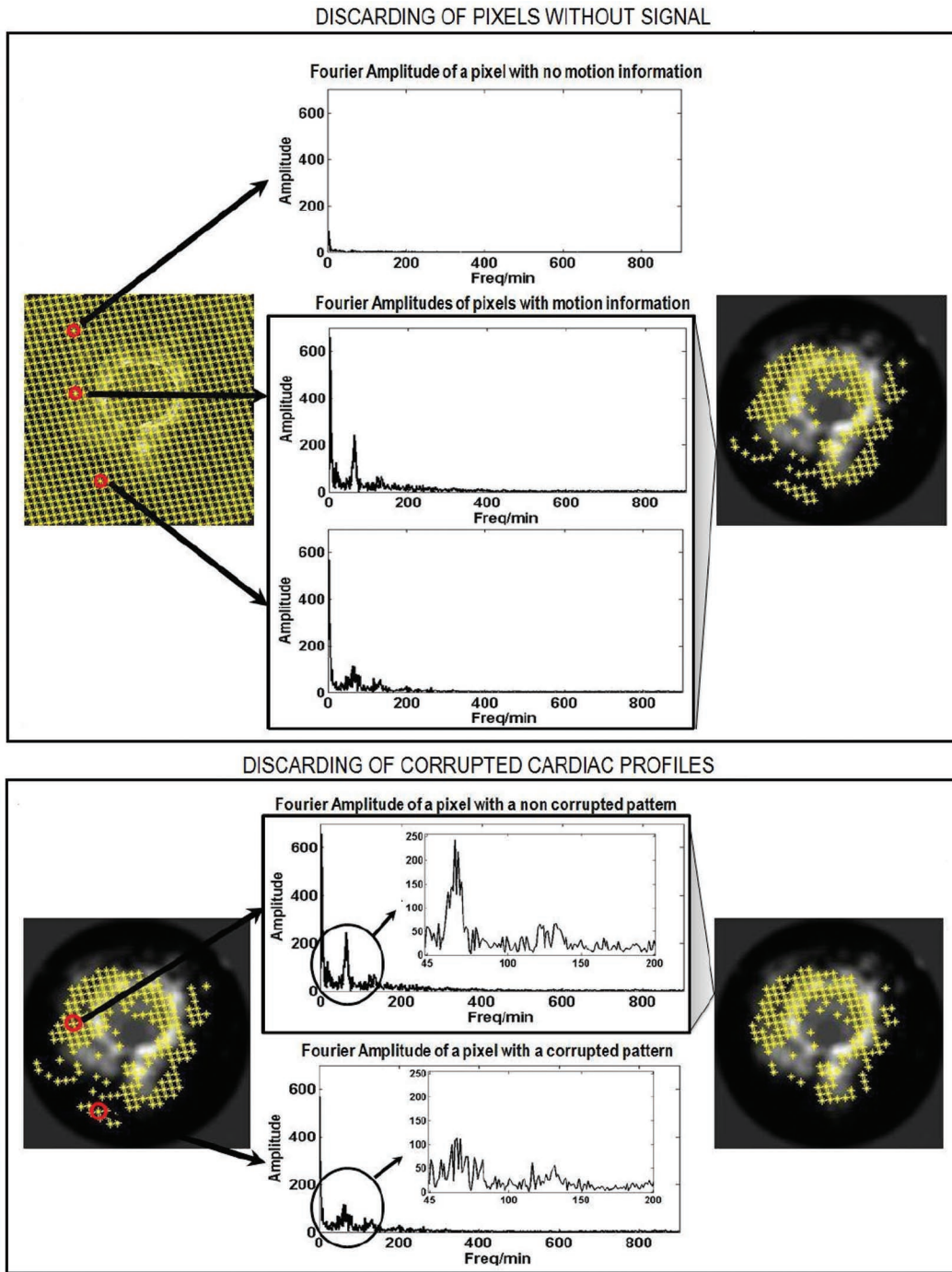



Fig. 4. Scheme illustrating the process of discarding pixels. The first step is discarding pixels with low signal in the local mean dynamic profile. The central plots correspond to the amplitudes of Fourier developments of a pixel with no motion information (top) and two pixels with motion information (bottom). The second step is the selection of pixels reflecting a well-defined cardiac profile. The central plots correspond to the amplitudes of Fourier developments of a pixel with a regular profile (top) and another one with a corrupted profile (bottom). 

whole sequence (E_{seq}) by averaging E^k over all sampled frames (N):

$$E_{\text{seq}} = \frac{1}{N} \sum_{k=1}^N E^k. \quad (3)$$

To compare our approach to existing methods, we have added the following quality scores: the difference between the number of frames manually and automatically gated

[9], [14] and fraction of the cardiac cycle of the algorithm-selected frames [9].

The difference in the number of sampled frames indicates the repetition rate (i.e., more than one sampling per cycle) of the method. Because a discrepancy of ± 1 is attributed to boundary conditions and is expected, we only report the number of segments (noted by RepRate) with a discrepancy over ± 1 frame. The fraction of cardiac cycle is defined for each frame as:

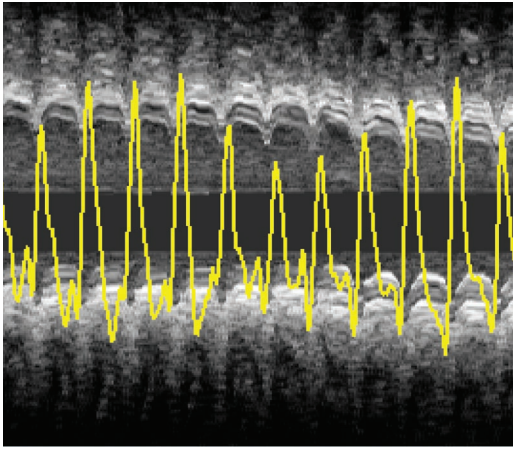


Fig. 5. Signal reflecting motion after averaging all local means selected by optical filter.

$$EF^k = \frac{E^k}{|s^k - s^{k+1}|}.$$

We note that EF^k is a measure similar to the fraction of R-R cycle reported in [9]. Like E^k , the values of EF^k for all frames provide a fraction function for each sequence. In this case, the quantity associated to the sequence is given by the standard deviation [9]:

$$EF_{\text{seq}} = 100 \frac{1}{N-1} \sum_{k=1}^N \left(EF^k - (1/N) \sum_{k=1}^N EF^k \right)^2. \quad (4)$$

We report two different statistics for comparing the performance of each method: ranges for quality scores and multiple comparison hypothesis test over E_{seq} . Statistical ranges of quality scores given by the mean \pm the variance for all sequences indicate the overall accuracy of each method. To detect if there are any significant differences

TABLE I. FILTER PARAMETERS.

$G_1: \{\sigma = 10\}$	$G_2: \{\sigma = 1.5\}$	$G_3: \{\sigma = 0.001\}$
$B_1: \{n = 1, \delta = 0.5\}$	$B_2: \{n = 1, \delta = 0.05\}$	$B_3: \{n = 1, \delta = 0.005\}$
$B_4: \{n = 2, \delta = 0.5\}$	$B_5: \{n = 2, \delta = 0.05\}$	$B_6: \{n = 2, \delta = 0.005\}$
$B_7: \{n = 4, \delta = 0.5\}$	$B_8: \{n = 4, \delta = 0.05\}$	$B_9: \{n = 4, \delta = 0.005\}$

among methods (that is, a best/worst performer), we have used the multiple comparison methodology proposed by Demsár in [26]. For each sequence (trial) the M filters (there are 12 in our case and might be considered as classifiers) are ranked according to their errors [given by (3)]. The ranking assigns 1 to the best performer and M for the worst one. The average ranks are statistically compared to find out if there are any significant differences. First, a multiple hypothesis test is computed to ensure that data are comparable. The null hypothesis states that all filters are equivalent. If the hypothesis is not rejected, the filters are not statistically different because either they have equal performance or there are not enough data sets. Otherwise, all filters are compared with each other by means of a Nemenyi test. The performance of two filters is significantly different if the corresponding average ranks differ by at least a critical difference given by the test.

IV. EXPERIMENTS

The methodologies were implemented in Matlab code (The MathWorks, Natick, MA) on a pc with a 3.20-GHz Pentium IV CPU (Intel Corp., Santa Clara, CA) and 1.50 GB of RAM. The average processing time per frame was 36 ms.

The set of parameters scanned for each filter family (Gaussian filters noted by G_i and Butterworth by B_i) are given in Table I. Fig. 6 shows the different filter profiles in the Fourier domain. Each plot corresponds to a differ-

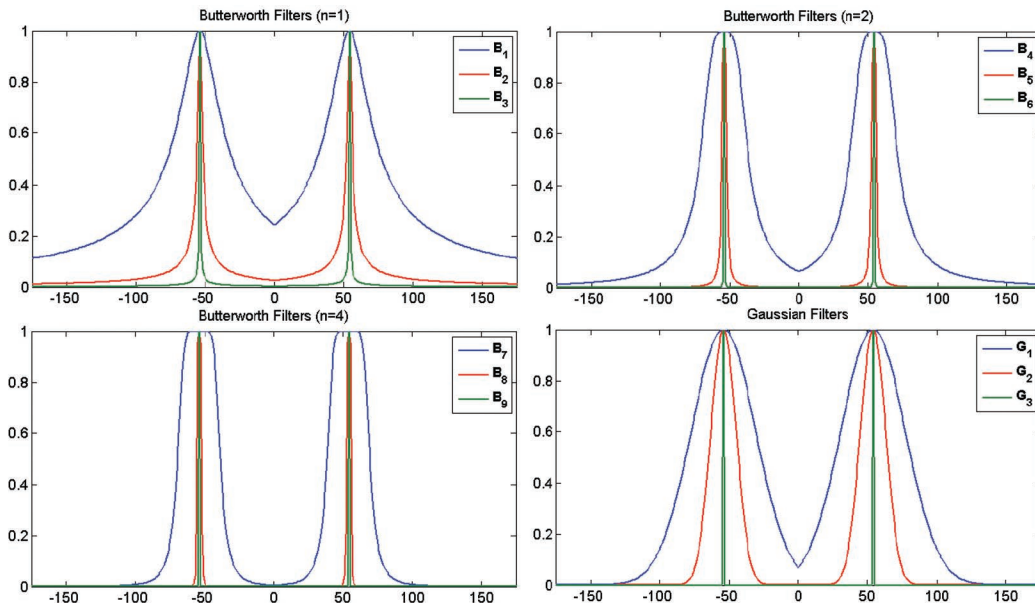


Fig. 6. Battery of filters gathered according to their bandwidth.

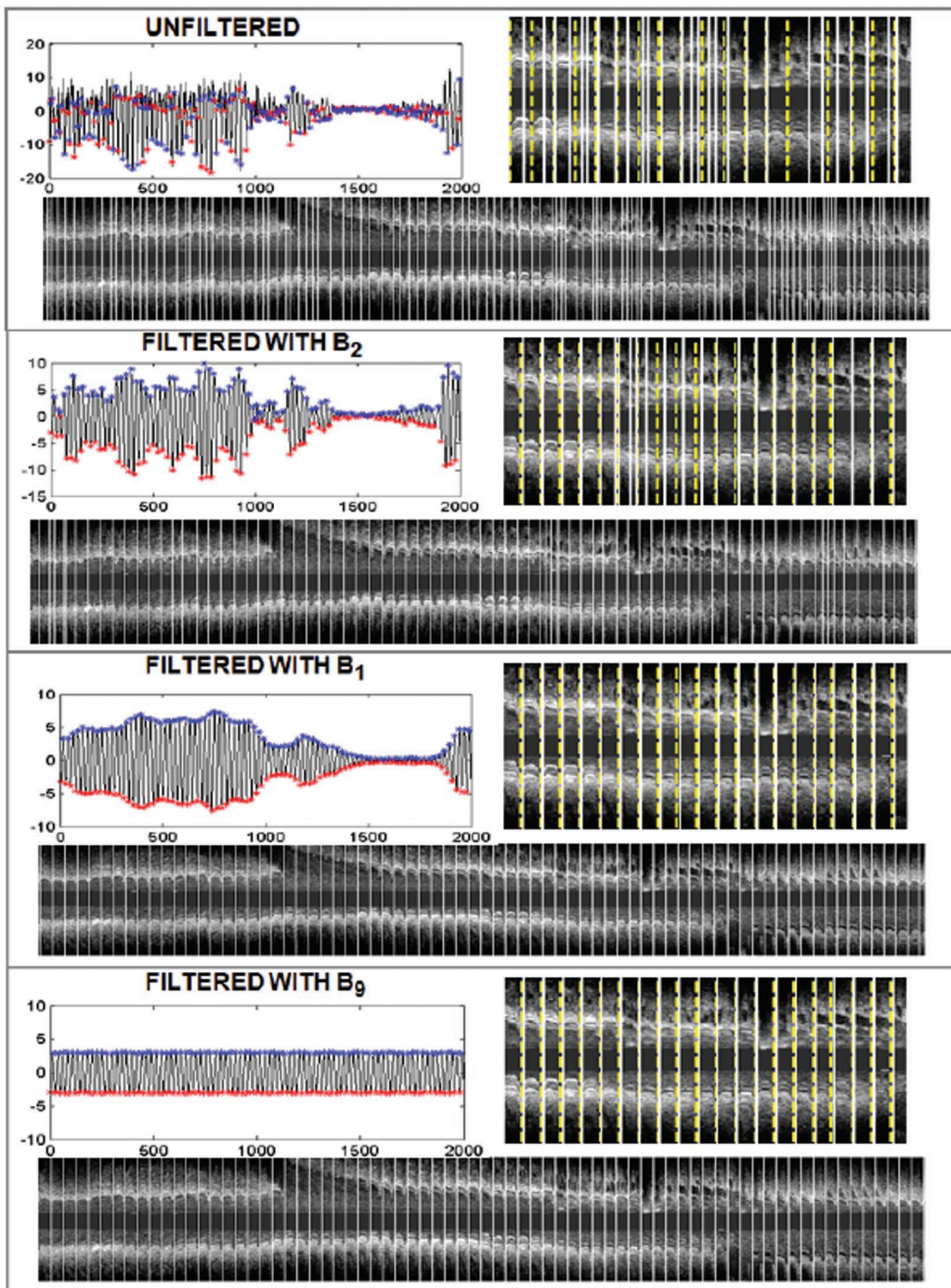



Fig. 7. Influence of band-pass filtering in cardiac phase retrieval for a regular case. Top-left images show the signals and the sampled extreme positions. Top-right images show the extreme position (solid lines) and the manual sampling (dashed lines). Bottom images show the extreme positions for the complete longitudinal cut. 

ent sub-family of filters: Gauss, Butterworth with $n = 1$, Butterworth with $n = 2$, and Butterworth with $n = 4$. For each sub-family, the filter with largest support is plotted in blue, the one with the medium support is shown in red and the smallest one is plotted in black. Vertical dashed lines indicate the frequency range around ω_c used for optical filtering ($\omega_c - \omega_c/2, \omega_c + \omega_c/2$).

Qualitative results of different filters and parameters are illustrated in Figs. 7 and 8 for sequences presenting

low (Fig. 7) and high (Fig. 8) variability in heart rate. We show results obtained by the unfiltered signal, the signal filtered with a broad-band filter (B_2), the signal filtered with a medium-band filter (B_1), and the signal filtered with a narrow-band filter (B_g). For each signal, we plot the signals with their extremes marked with crosses (red for minimums and blue for maximums) in the top-left graphics, with x -axis representing frames and the y -axis representing LM-filtered intensity. The frames sampled at maximums are

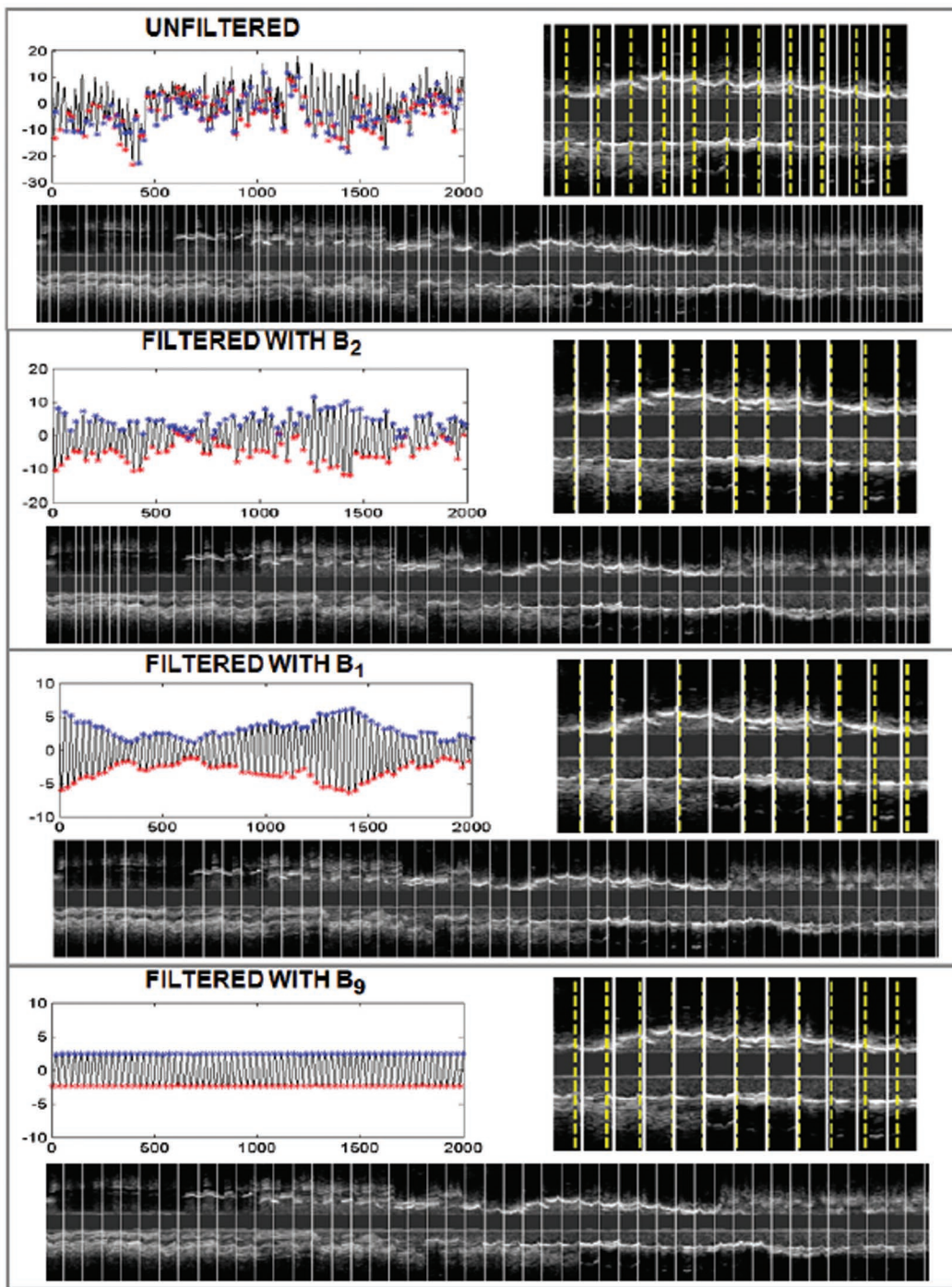



Fig. 8. Influence of band-pass filtering in cardiac phase retrieval for an irregular case. Top-left images show the signals and the sampled extreme positions. Top-right images show the extreme position (solid lines) and the manual sampling (dashed lines). Bottom images show the extreme positions for the complete longitudinal cut. 

indicated with vertical lines on the longitudinal cuts shown at the bottom of each graphic. Finally the extreme position together with the manual frame detections are shown in the longitudinal cuts close-up images on the top right-hand side. Extreme positions of signals are plotted in solid white lines and manual detections in dashed yellow lines.

In both images, extreme positions of the unfiltered signal produce an over-sampling due to the impact of high

frequencies. Signals filtered with a narrow-band filter produce a regular periodic sampling suitable for cases with a low variability in heart rate, but are unable to capture variations caused by non-constant heart rate (images labeled B_0 in both figures). However, broad-band filters produce better results for high variability in heart rate, although they might over-sample regular sequences (images labeled B_2 in both figures). The band-pass filter achiev-

TABLE II. QUANTITATIVE RESULTS FOR THE FILTERS SELECTED BY THE NEMENYI TEST.

Filter	E_{seq} (frames)	E_{seq} (s)	E_{seq} (mm)	EF_{seq} (%)	RepRate
G_1	3.8644 ± 1.7497	0.1288 ± 0.0583	0.0644 ± 0.0292	9.4705 ± 4.8763	1
G_2	3.8929 ± 1.6648	0.1298 ± 0.0555	0.0649 ± 0.0277	10.2111 ± 4.5102	2
B_1	4.0240 ± 1.6105	0.1341 ± 0.0537	0.0671 ± 0.0268	10.9402 ± 4.7388	10
B_2	3.8972 ± 1.8001	0.1299 ± 0.0600	0.0650 ± 0.0300	8.4289 ± 4.9313	1
B_3	4.4488 ± 1.9458	0.1483 ± 0.0649	0.0741 ± 0.0324	8.3204 ± 4.2297	0
B_4	3.8570 ± 1.7338	0.1286 ± 0.0578	0.0643 ± 0.0289	9.9875 ± 4.7239	2
B_5	4.1506 ± 1.8597	0.1384 ± 0.0620	0.0692 ± 0.0310	8.6898 ± 4.5845	1
B_7	3.8680 ± 1.7279	0.1289 ± 0.0576	0.0645 ± 0.0288	9.9836 ± 4.6334	1
B_8	4.2071 ± 1.8385	0.1402 ± 0.0613	0.0701 ± 0.0306	8.6713 ± 4.6943	1

TABLE III. AVERAGE RANK OF THE FILTERS FOR NEMENYI TEST.

Filter	G_1	G_2	G_3	B_1	B_2	B_3	B_4	B_5	B_6	B_7	B_8	B_9
Rank	5.9091	5.6591	8.2727	6.8864	4.9318	6.6136	5.9091	5.6591	8.3182	5.8409	5.7727	8.2273

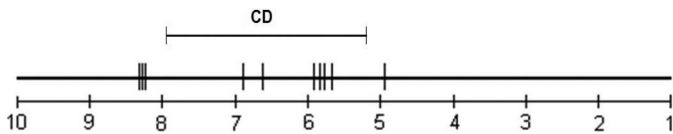


Fig. 9. Comparison of different filters. Sorted average ranks from best (right) to worst (left) used for the Nemenyi test.

ing a better compromise is the middle-band one (images labeled B_1 in both figures).

Table II reports the average ranks reflecting (the smaller, the better) each filter's performance. For a significance level of 0.1, the Nemenyi critical difference (CD) is 3.86. The test detects that Butterworth filters with $n = 2$ and 4, $\delta = 0.005$ (B_6 and B_9) and Gaussian with $\sigma = 0.001$ (G_3), which are too restricted around ω_c , are significantly worst. The Nemenyi test also reports that there is not enough evidence of a significantly different performance among the remaining methods. Fig. 9 shows the filters' average ranks from best (right) to worst (left) together with the critical difference, to visually compare all filters.

Table III reports statistical ranges for the filters achieving better ranks. The table reports ranges for E_{seq} in frames, seconds, and millimeters; ranges for EF_{seq} ; and

the repetition rate, RepRate. With the exception of the filter with largest support (B_1), all filters present a low oversampling rate (at most 2). Although differences are not significant, the Butterworth filter B_2 ($n = 1$, $\delta = 0.05$) achieves the best results with E_{seq} within 3.89 ± 1.80 frames (which corresponds to 0.06 ± 0.03 mm) and EF_{seq} for cardiac fraction within $8.43 \pm 4.93\%$.

Fig. 10 shows the performance for the best configuration in 2 large longitudinal cuts. The original cuts obtained by considering all sequence frames are shown in the left images. The top segment presents the characteristics saw-tooth shape in longitudinal profiles induced by heart beat. The bottom cut also contains a discontinuous calcium plaque at the first upper half of the sequence. The cuts obtained by sampling frames at the extreme (maximums) positions of the signal filtered with B_2 are shown in the right images. For both cases, the ECG-sampled images show continuous profiles for lumen contours. In particular, the calcium plaque has stabilized in the second segment.

V. DISCUSSION

Cardiac phase retrieval and compensation is a key feature for accurate 3-D exploring of coronary arteries in

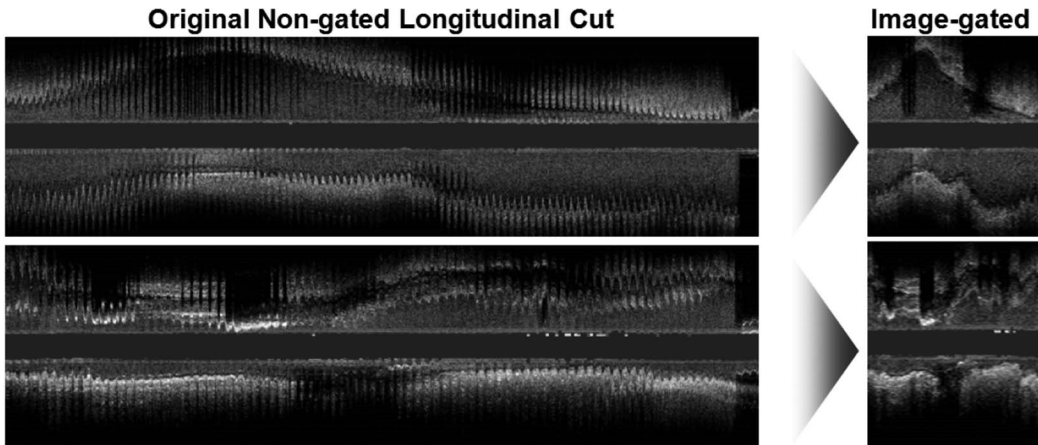


Fig. 10. Results of image-based ECG sampling for two different longitudinal cuts.

IVUS sequences. Because cardiac phase can be strongly affected by artery lesions and other cardiac factors, we consider that the following issues should be discussed.

A. Comparison to Existing Methods

The first methods developed for retrospective ECG-gating [3], [4] were mainly concerned with comparing off-line sampling of sequences to on-line ECG-triggered acquisitions. To do so, they reported comparisons between volumetric measures obtained using both methodologies. A main concern is that such validation protocol requires ECG-gating systems for prospective image capture, which are not always available and increase acquisition time up to three times [4].

In the absence of ECG-gated acquisitions, a standard well-defined methodology for comparing gating algorithms (image-based or not) is not available, especially in the absence of an ECG-signal. Many methods based on quality assessment of longitudinal cuts appearance [13], [17], [20] and those reporting quantitative numbers do not follow a standard protocol [9], [14]. Such heterogeneity in validation protocols makes faithful comparison across methods a difficult task. Also, given that there are no public IVUS databases, any comparison is merely illustrative, because reported statistics are computed from different data sets.

The error ranges for cardiac fraction (EF_{seq}) obtained by the best performer (8.43 ± 4.93) compare with the ranges, within 8.08 ± 3.11 , given in [9]. The increase in standard deviation might be attributed to the different number of samples of the databases considered (22 in our case versus 4 in [9]). To compare our method to the single *in vivo* case reported in [14], we have computed signed distances for the best filter. In such a case, the average reflects the shift between automatic and manual samplings, and the quality score reflecting the accuracy of the method is the standard deviation along the sequence, because it reflects the variability of the sampling. We significantly outperform the range -10 ± 74 ms in 7 cases (representing 31.82% of our data) with a best range of 88.46 ± 22.98 ms. In fact, the average standard deviation in 16 cases (72.73%) is in the range within 74.35 ± 39.48 ms. The remaining cases are outliers that fit into one of the categories described in the limitations subsection (Section V-E).

Concerning complexity, our local approach is $\mathcal{O}(n)$, where n is the number of frames in the sequence analyzed. This constitutes a significant reduction in complexity, compared with methods based on dissimilarity matrices [9], [17], which are $\mathcal{O}(n^2)$. Furthermore, we achieve a high performance in speed (close to real time) with 36 ms per frame on average.

B. Performance on Rigid Segments

Different factors such as heart pumping, blood pressure, or artery geometric properties mainly contribute to the dynamics of coronary arteries [20], [27], [28]. The first-order approximation to vessel dynamics is given by a linear transformation combining two main deformations: rigid (translation and rotation) and elastic (radial scaling)

[29]. In the case of human coronary arteries, scaling is very close to 1 [30]. It follows that the main contributions to vessel cardiac dynamics are given by the rigid part of such approximation.

By their physical properties, calcified areas (like stented arteries) are rigid structures. It follows that their motion is almost lacking in elastic radial scaling, but still includes rigid contributions (translation and rotation), which are the predominant motions. It follows that, although pixels inside plaque seem motionless, image pixels on the angular transition between calcium and soft tissue reflect in-plane rotation. In a similar way, pixels on 3-D longitudinal transitions (i.e., transitions along the sequence) reflect longitudinal motion. Therefore, bordering points on rigid vessel structures reflect cardiac motion and are good candidates for retrieving cardiac phase.

Our data set includes 9 stented segments; the accuracy for these segments (using the best filter, B_2) is 3.9986 ± 1.7852 frames, and thus compares to the overall accuracy.

C. Impact of In-Plane Motion

The complex motion of the imaging catheter inside the coronary vessel causes two main motion artifacts in IVUS sequences: 1) in-plane rigid motion (vessel-catheter translation and rotation), and 2) forward and backward longitudinal motion along the catheter axis [1]. Although the influence of these phenomena on the evolution of the vessel wall pixels cannot be clearly decoupled, both reflect cardiac phase in the same manner. Therefore, any quantity reflecting image changes induced by any of them is suitable for the task of cardiac phase retrieval. This is the case for all image-based methods which compute a signal that captures the changes in sequence frames (such as lumen area [13] or image misalignment [9], [14]) that cardiac motion induces, regardless of its nature (in- or out-of-plane).

D. Impact of Variability of Heart Beat

Concerning high variability in heart rate, we recall that any variation in heart rate spreads the frequencies of the Fourier series around the theoretical harmonic. This produces a harmonic peak including all frequencies that contribute to the principal periodic motion along the sequence. The more irregularities in periodicity we have, the more spread around the theoretic harmonic the Fourier development is. It follows that heart rate variability influences the decay and support of the band-pass filter, which should include all frequencies contributing to the periodic component of the signal.

According to our experiments, as long as there is not a substantial sudden change in heart rate, the critical criterion for an accurate cardiac phase retrieval is the band-pass filter support, rather than its decay. A preliminary study shows that, for a given decay (Butterworth with $n = 1$) there are significant differences between large (over

optical filtering support given by $\delta = 1$), medium (within optical filtering support given by $\delta = 0.05$), and small (restricted to ω_c given by $\delta = 0.001$) supports with Nemenyi critical difference equal to 0.6187 and average ranks equal to 2.4318, 1.3636, and 2.2045, respectively.

This might not be the case for subjects presenting large and sudden changes in heart rate. We plan to extend the set of patients to cases presenting a significantly irregular cardiac profile, to determine the role of the filter decay.

E. Limitations

A main limitation of image-based gating methods is that they require an apparent cardiac motion along IVUS sequences. Consequently, accuracy of cardiac phase retrieval is prone to decrease at segments on infarcted hearts presenting a drastically reduced cardiac motion. Given that pathological groups have not been distinguished in our experiments, this might be a main source of error, with an impact on performance that has not been identified.

Another source of error in current image-based methods is that they rely on changes observed in sequence intensity. We consider that the quality of IVUS images naturally bounds accuracy of intensity-based methods. It follows that current approaches (including ours) are unable to produce samplings synchronized to the shortest cardiac phases (isovolumetric contraction and relaxation). Both phases last between 30 and 70 ms [31], which would imply an average error between ± 1 and ± 2 frames. We are currently exploring alternative quantities to image intensity evolution based on vessel dynamics.

A main limitation of our validation protocol is the manual sampling of sequences, because it is prone (because of the quality of longitudinal cuts) to present a high inter- and intra- observer variability. This might introduce a source of variability in statistics and it is a main drawback for fine tuning of the filter profile. An on-going work is gathering a database with ECG signals large enough for a better design of the filter profile.

VI. CONCLUSIONS

In this paper, we propose a method for extracting cardiac signal from analysis of IVUS images and we explore the ability of a battery of filters to remove noise and other non-cardiac phenomena. The cardiac signal is based on the evolution of tissue density of mass (given by image local mean). The filters considered cover different bandwidths (centered at the cardiac phase, ω_c) and decays.

Local approaches present several advantages over methods based on global similarity measures. The accuracy compares to existing approaches but significantly reduces computational complexity. Our local method also performs equally well on stented segments, which shows its potential for clinical applicability.

Concerning the band-pass filter profile, several interesting conclusions are derived from our experiments. The

band-pass filter's support should not be too restricted around ω_c to avoid uniform samplings. Also, a large support is prone to produce sampling with a high repetition rate. We have observed that filters with support in the range considered for optical filtering (given by vertical lines in Fig. 6) achieve optimal performances. A preliminary trial indicates that the range $(\omega_c - \omega_c/2, \omega_c + \omega_c/2)$ is a good candidate for the filter support.

Because the bandwidth of the filter is related to the variability in the heart rate, the performance of the filters on segments with a regular cardiac phase and with an irregular cardiac phase could be significantly different. We plan to extend the set of patients to cases presenting a significantly irregular cardiac profile, to determine whether this is a critical issue.

ACKNOWLEDGMENTS

We thank the Heart Institute (InCor) do Hospital das Clínicas da Faculdade de Medicina da Universidade de São Paulo for their support with the IVUS images database.

REFERENCES

- [1] A. Arbab-Zadeh, A. N. DeMaria, W. F. Penny, R. J. Russo, B. J. Kimura, and V. Bhargava, "Axial movement of the intravascular ultrasound probe during the cardiac cycle: Implications for three-dimensional reconstruction and measurements of coronary dimensions," *Am. Heart J.*, vol. 138, no. 5, pt. 1, pp. 865–872, 1999.
- [2] C. von Birgelen, G. S. Mintz, A. Nicosia, D. P. Foley, W. J. van der Giessen, N. Bruining, S. G. Airiian, J. R. Roelandt, P. J. de Feyter, and P. W. Serruys, "Electrocardiogram-gated intravascular ultrasound image acquisition after coronary stent deployment facilitates on-line three-dimensional reconstruction and automated lumen quantification," *J. Am. Coll. Cardiol.*, vol. 30, no. 2, pp. 436–443, 1997.
- [3] S. A. de Winter, R. Hamers, M. Degertekin, K. Tanabe, P. A. Lemos, P. W. Serruys, J. R. Roelandt, and N. Bruining, "Retrospective image-based gating of intracoronary ultrasound images for improved quantitative analysis: The Intelligate method," *Catheter. Cardiovasc. Interv.*, vol. 61, no. 1, pp. 84–94, 2004.
- [4] C. von Birgelen, C. D. Mario, W. Li, J. C. Schuurbiens, C. J. Slager, P. J. de Feyter, J. R. Roelandt, and P. W. Serruys, "Morphometric analysis in three-dimensional intracoronary ultrasound: An *in vitro* and *in vivo* study performed with a novel system for the contour detection of lumen and plaque," *Am. Heart J.*, vol. 132, no. 3, pp. 516–527, 1996.
- [5] Y. Shi, F. J. de Ana, S. J. Chetcuti, and M. O'Donnell, "Motion artifact reduction for IVUS-based thermal strain imaging," *IEEE Trans. Ultrason. Ferroelectr. Freq. Control*, vol. 52, no. 8, pp. 1312–1319, 2005.
- [6] C. L. Korte, A. F. W. van der Steen, E. I. Céspedes, and G. Pasterkamp, "Intravascular ultrasound elastography of human arteries: Initial experience *in vitro*," *Ultrasound Med. Biol.*, vol. 24, no. 3, pp. 401–408, 1998.
- [7] K. Y. E. Leung, R. A. Baldewising, F. Mastik, J. Schaar, and D. Gisolf, "Motion compensation for intravascular ultrasound palpography," *IEEE Trans. Ultrason. Ferroelectr. Freq. Control*, vol. 53, no. 7, pp. 1269–1280, 2006.
- [8] M. G. Danilouchkine, F. Mastik, and A. F. W. van der Steen "Improving IVUS palpography by incorporation of motion compensation based on block matching and optical flow," *IEEE Trans. Ultrason. Ferroelectr. Freq. Control*, vol. 55, no. 11, pp. 2392–2404, 2008.
- [9] S. M. O'Malley, J.F. Granada, S. Carlier, M. Naghavi, and I. A. Kakadiaris, "Image-based gating of intravascular ultrasound pull-back sequences," *IEEE Trans. Inf. Technol. Biomed.*, vol. 12, no. 3, pp. 299–306, 2008.

- [10] B. Lu, S.-S. Mao, N. Zhuang, H. Bakhsheshi, H. Yamamoto, J. Takasu, S. C. Liu, and M. J. Budoff, "Coronary artery motion during the cardiac cycle and optimal ECG triggering for coronary artery imaging," *Invest. Radiol.*, vol. 36, no. 5, pp. 250–256, 2001.
- [11] N. Bruining, C. von Birgelen, P. J. de Feyter, J. Ligthart, W. Li, P. W. Serruys, and J. R. T. C. Roelandt, "ECG-gated versus nongated three-dimensional intracoronary ultrasound analysis: Implications for volumetric measurements," *Cathet. Cardiovasc. Diagn.*, vol. 43, no. 3, pp. 254–260, 1998.
- [12] S. Nadkarni, D. Boughner, and A. Fenster, "Image-based cardiac gating for three-dimensional intravascular ultrasound imaging," *Ultrasound Med. Biol.*, vol. 31, no. 1, pp. 53–63, 2005.
- [13] H. Zhu, K. D. Oakeson, and M. H. Friedman, "Retrieval of cardiac phase from IVUS sequences," in *Medical Imaging 2003: Ultrasonic Imaging and Signal Processing*, 2003, pp. 135–146.
- [14] M. M. S. Matsumoto, P. A. Lemos, T. Yoneyama, and S. S. Furuie, "Cardiac phase detection in intravascular ultrasound images," *Proc. SPIE*, vol. 6920, no. 1, art. no. 69200D, Feb. 2008.
- [15] S. M. O'Malley, S. G. Carlier, M. Naghavi, and I. A. Kakadiaris, "Image-based frame gating of IVUS pullbacks: A surrogate for ECG," in *Proc. IEEE Int. Conf. Acoustics, Speech, and Signal Processing*, 2007, pp. 433–436.
- [16] S. M. O'Malley, M. Naghavi, and I. A. Kakadiaris, "Image-based frame gating for contrast-enhanced IVUS sequences," in *Int. Workshop Computer Vision for Intravascular and Intracardiac Imaging*, 2006, pp. 15–22.
- [17] C. Gatta, O. Pujol, R. Leor, J. M. Ferre, and P. Radeva, "Robust image-based IVUS pullbacks gating," in *11th Int. Conf. Medical Image Computing and Computer-Assisted Intervention*, 2008, pp. 518–525.
- [18] A. Hernández-Sabaté, D. Gil, E. F. Nofrerias, P. Radeva, and E. Martí, "Approaching rigid artery dynamics in IVUS," *IEEE Trans. Med. Imaging*, vol. 28, no. 11, pp. 1670–1680, 2009.
- [19] J. A. Shaw, B. A. Kingwell, A. S. Walton, J. D. Cameron, P. Pillay, C. D. Gatzka, and A. M. Dart, "Determinants of coronary artery compliance in subjects with and without angiographic coronary artery disease," *J. Am. Coll. Cardiol.*, vol. 39, no. 10, pp. 1637–1643, 2002.
- [20] S. Nadkarni, H. Austin, G. Mills, D. Boughner, and A. Fenster, "A pulsating coronary vessel phantom for two and three-dimensional intravascular ultrasound studies," *Ultrasound Med. Biol.*, vol. 29, no. 4, pp. 621–628, 2003.
- [21] A. Klug and D. J. DeRosier, "Optical filtering of electron micrographs: Reconstruction of one-sided images," *Nature*, vol. 212, no. 5057, pp. 29–32, 1966.
- [22] D. Gil, O. Rodriguez-Leor, P. Radeva, and J. Mauri, "Myocardial perfusion characterization from contrast angiography spectral distribution," *IEEE Trans. Med. Imaging*, vol. 27, no. 5, pp. 641–649, 2008.
- [23] A. Hernández-Sabaté, D. Rotger, and D. Gil, "Image-based ECG sampling of IVUS sequences," in *IEEE Int. Ultrasonics Symp.*, 2008, pp. 1330–1333.
- [24] A. Hernández and D. Gil, "How do conservation laws define a motion suppression score in *in vivo* IVUS sequences?" in *IEEE Int. Ultrasonics Symp.*, 2007, pp. 2231–2234.
- [25] S. G. Mallat, *A Wavelet Tour of Signal Processing*. New York, NY: Academic Press, 1998.
- [26] J. Demsar, "Statistical comparisons of classifiers over multiple data sets," *J. Mach. Learn. Res.*, vol. 7, pp. 1–30, 2006.
- [27] J. Mazumdar, *Biofluids Mechanics*. Singapore: World Scientific Publishing, 1992.
- [28] G. Holzapfel, T. Gasser, and M. Stadler, "A structural model for the viscoelastic behavior of arterial walls: Continuum formulation and finite element analysis," *Eur. J. Mech. A*, vol. 23, no. 3, pp. 1–162, 2002.
- [29] E. Waks, J. Prince, and S. Andrew, "Cardiac motion simulator for tagged MRI," in *Proc. Workshop on Mathematical Methods in Biomedical Image Analysis*, 1996, p. 182.
- [30] M. D. R. Ramírez, "A physics-based image modelling of IVUS as a geometric and kinematics system," Ph.D. thesis, Computer Science Dept., Universitat Autònoma de Barcelona, 2005.
- [31] Y. Notomi, M. G. Martin-Miklovic, S. J. Oryszak, and T. Shiota et al. "Enhanced ventricular untwisting during exercise: A mechanistic manifestation of elastic recoil described by doppler tissue imaging," *Circulation*, vol. 113, no. 21, pp. 2524–2533, 2006.



Aura Hernández-Sabaté received her degree in mathematics from Universitat Autònoma de Barcelona (UAB, Bellaterra, Spain) in 2002. In 2005 and 2009, respectively, she received her M.Sc. and Ph.D. degrees in computer science from the UAB. She is a lecturer at UAB and collaborates with the Computer Vision Center, (www.cvc.uab.es). Her research interests are focused on image processing techniques for biomedical images, such as segmentation and dynamical parameters estimation, and mathematical models for biomedical image processing, like contour geometry, geometric flows, and variational models.



Debora Gil received her degree in mathematics from Universitat de Barcelona in 1994 and her Ph.D. from Universitat Autònoma de Barcelona (UAB, Bellaterra, Spain) in 2004. Since 1997, she's been working for the Computer Vision Center (CVC) and the Computer Science Department of Universitat Autònoma de Barcelona. She has been in charge of the Modelling and Visualization group in CVC since 2007. Her main interests are mathematical tools applied to image processing (especially, but not exclusively, biomedical imag-

ing) and she has expertise in pde-based methods, segmentation, motion analysis, and shape modeling.

Jaume Garcia-Barnés and **Enric Martí** photographs and biographies unavailable at time of publication.